Dalton Transactions

ROYAL SOCIETY OF CHEMISTRY

PAPER

View Article Online
View Journal | View Issue

Cite this: *Dalton Trans.*, 2025, **54**, 1871

$Sr_3Zr_2Cu_4Q_9$ (Q = S and Se): two novel layered quaternary mixed transition metal chalcogenides†

Sayani Barman, [a] Sweta Yadav, [a] Akshay K. Ray, [a] Swati,[a] M. Deepa, [a] Manish K. Niranjan[b] and Jai Prakash *[a]

Depending on their bandgaps, mixed metal layered chalcogenides are potential candidates for thermoelectric and photovoltaic applications. Herein, we reported the exploratory synthesis of Sr–Zr–Cu–Q (Q = S/Se) systems, resulting in the identification of two novel quaternary chalcogenides: $Sr_3Zr_2Cu_4S_9$ and $Sr_3Zr_2Cu_4Se_9$. These isoelectronic compounds ($Sr_3Zr_2Cu_4Q_9$) crystallized in two different structural types. The $Sr_3Zr_2Cu_4S_9$ structure (space group: $P\bar{1}$) adopted the $Ba_3Zr_2Cu_4S_9$ structure type with eighteen unique atomic sites: 3 × Sr, 2 × Zr, 4 × Cu, and 9 × S. In contrast, the $Sr_3Zr_2Cu_4Se_9$ structure ($P\bar{1}$) represented a unique structure type with nineteen unique atomic positions including one additional Cu site compared to the $Sr_3Zr_2Cu_4S_9$ structure. The sulfide structure was stoichiometric, whereas the selenide structure was found to be non-stoichiometric with three partially occupied Cu positions. The $Sr_3Zr_2Cu_4Q_9$ structures consisted of $^{\infty}_{2}[Zr_2Cu_4Q_9]^{6-}$ layers with the Sr^{2+} cations occupying the interstitial spaces. In both structures, the Zr atoms occupied distorted octahedral positions. A striking difference between the two structures resulted from the distinct bonding interactions between the Cu and Q atoms. The optical bandgap of polycrystalline $Sr_3Zr_2Cu_4S_9$ was 1.7(1) eV. Interestingly, resistivity measurements of polycrystalline $Sr_3Zr_2Cu_4Se_9$ revealed metallic/degenerate semiconducting behavior at low temperatures. The photovoltaic performance of semiconducting $Sr_3Zr_2Cu_4S_9$ demonstrated ~24% increment in power conversion efficiency when incorporated into a TiO_2/CdS photoanode due to its narrower bandgap, which increased the light-harvesting ability of the cell. We also explored the theoretical electronic structures, COHP, and Bader charges of the $Sr_3Zr_2Cu_4Q_9$ structures using DFT calculations.

Received 20th October 2024,
Accepted 3rd December 2024

DOI: 10.1039/d4dt02928c

rsc.li/dalton

1. Introduction

Inorganic multinary chalcogenide compounds, featuring two or more types of metals/metalloids and chalcogen elements (Q), such as sulfur, selenium, and tellurium, represent a fascinating class of materials. Their tunable compositions and structural flexibility enable the tailoring of physical properties for a wide range of technological applications. Therefore, chalcogenides have emerged as potential materials for a variety of applications, such as high-temperature superconductivity,[1,2] photovoltaics,[3,4] catalysis,[5,6] thermoelectric properties,[7,8] and non-linear optics.[9–12] Unlike binary counterparts, multinary chalcogenides allow the incorporation of multiple metals and chalcogen atoms, opening a vast design space to tailor their properties. This flexibility allows for fine-tuning of the energy difference between the electron-filled and empty states, thereby influencing their electrical and thermal conductivity, light absorption, and emission. Many chalcogenides are also well known for their sensitivity to light and other stimuli, making them ideal candidates for use in advanced sensors and imaging technologies.[13–16]

Copper-containing chalcogenides, especially sulfides and selenides, are emerging materials for photovoltaic and thermoelectric (TE) applications due to their non-toxicity and earth abundance.[4,17–20] The high mobility of Cu^{1+} ions in these multinary chalcogenide structures is well known in compounds such as $Cu_{2-x}Se$,[21] Cu_7PSe_6,[22] $CuCrSe_2$,[23] and AgCuSe.[24] However, some of these structures are unstable at higher temperatures due to the migration of Cu ions within their crystal lattices (*e.g.*, $Cu_{2-x}Se$).[25,26] Unlike copper oxides, the Cu atoms in chalcogenides exist in the monovalent state and are mostly four-coordinated with a tetrahedral coordination geometry. Notable examples of such compounds include $BaCu_{6-x}SeTe_6$,[27] $BaLnCuS_3$ (Ln = Pr, Sm, Dy, Ho, Yb),[28,29] and Cu_4SnS_4.[30] In these structures, alkali (A) and alkaline-earth (Ak) metals func-

[a]*Department of Chemistry, Indian Institute of Technology Hyderabad, Kandi, Sangareddy, Telangana 502284, India. E-mail: jaiprakash@chy.iith.ac.in*
[b]*Department of Physics, Indian Institute of Technology Hyderabad, Kandi, Sangareddy, Telangana 502284, India*

†Electronic supplementary information (ESI) available: Additional crystallographic details of the $Sr_3Zr_2Cu_4S_9$ and $Sr_3Zr_2Cu_4Se_9$ structures. CCDC 2390675 and 2390676. For ESI and crystallographic data in CIF or other electronic format see DOI: https://doi.org/10.1039/d4dt02928c

tion as electron donors and exhibit higher coordination numbers than the transition metals. The A^{1+} or Ak^{2+} ions in these compounds can be replaced with lower or higher valent chemical dopants to control the number of charge carriers. Also, many of these multinary chalcogenides offer low intrinsic thermal conductivity values due to their complex structures and chemical bonding. Therefore, the Cu-containing multinary chalcogenides with narrow bandgaps are actively pursued for their potential thermoelectric applications. Examples of such compounds are $ACuZrQ_3$ [31] and $BaSc_{1-x}Gd_xCuTe_3$.[32]

Moreover, the tunable bandgaps of the Cu/Ag-containing chalcogenides also make them potential candidates for solar cells, light-emitting diodes (LEDs), and photocatalysis applications. As discussed earlier, thanks to the high mobility of copper or silver atoms in these semiconducting chalcogenides, additional electronic levels close to the valence band are present in these compounds, making them efficient in electron transfer rather than hole recombination on sunlight absorption.[33,34] $BaCu_2SnS_{4-x}Se_x$,[35] $CuGaSe_2$,[36] $CuSbS_2$,[37] $BaCeCuS_3$,[38] Cu_2ZnSnQ_4 (Q = S, Se),[39] and $CuIn_xGa_{1-x}(S_xSe_{1-x})_2$ [40] are a few examples of such chalcogenide materials with excellent photovoltaic power conversion efficiencies. $CuSbS_2$ [37] is one of the chalcogenides actively explored for photovoltaics and thermoelectric applications.

Therefore, many research groups worldwide have been actively synthesizing new Cu/Ag-containing multinary chalcogenides with semiconducting properties to identify new potential materials for solar cells and *TE* applications. We have produced several novel complex metal chalcogenides in our quest to develop new semiconducting compounds for *TE* and solar cell applications; these include 12-$BaBi_2S_4$,[41] $Ba_8Zr_2Se_{11}(Se_2)$,[42] and $BaCeCuS_3$.[38] In this work, we report the synthesis of two novel compounds, namely, $Sr_3Zr_2Cu_4S_9$ and $Sr_3Zr_2Cu_4Se_9$, with layered structures. $Sr_3Zr_2Cu_4S_9$ is the first quaternary phase in the Sr–Zr–Cu–S system, while $Sr_3Zr_2Cu_4Se_9$ is the second member of the Sr–Zr–Cu–Se system for which only the quaternary phase, $Sr_{0.5}CuZrSe_3$,[43] is reported. $Sr_3Zr_2Cu_4Se_9$ represents a new structure type. We have studied the structural aspects and physical properties of $Sr_3Zr_2Cu_4Q_9$ compounds. Thermoelectric properties of $Sr_3Zr_2Cu_4Se_9$, a semimetal/degenerate semiconductor, are explored in detail. The $Sr_3Zr_2Cu_4S_9$ sulfide, a semiconductor with an optical bandgap of 1.7(1) eV, is explored for photovoltaic applications. Incorporating the quaternary title sulfide phase in a TiO_2/CdS photoanode shows a 24% increment in the power conversion efficiency of the fabricated solar cell. The electronic band structures of the $Sr_3Zr_2Cu_4Q_9$ phases are studied using the DFT method.

2. Experimental section

2.1 Chemicals used and synthetic methodologies

$Sr_3Zr_2Cu_4S_9$ and $Sr_3Zr_2Cu_4Se_9$ phases were synthesized using S/Se powder, Cu powder, Zr rod, and Sr granules. All these elements were procured from Sigma Aldrich with purities ≥99.5%. The Sr granules were cut into smaller pieces, and the zirconium rod was filed into powder for the reactions. Unless stated otherwise, all the chemicals are handled inside a glove box filled with argon gas.

We used the SnO_2 : F (FTO) coated glass substrates (Pilkington) with a sheet resistance of ~25 Ω cm^{-2} to fabricate solar cells for photovoltaic studies. Other chemicals (reagent grade) used for preparing the solar cells and photovoltaic measurements are the following: TiO_2 P25 powder, fumed silica and Ni-foam were procured from Evonik, Cabosil, and Gelon, respectively, and cadmium acetate, sodium sulfide, titanium tetrachloride, methanol, toluene, Triton X-100, acetylacetone, multi-walled carbon nanotubes (MWCNTs), polyvinylidene fluoride (PVdF), carbon black (CB), and *N*-methyl-2-pyrrolidone (NMP) were purchased from Merck and used directly.

2.1.1 Syntheses of $Sr_3Zr_2Cu_4Q_9$ (Q = S and Se) crystals. The elements (Sr, Zr, Cu, and Q) were reacted at high temperatures to prepare $Sr_3Zr_2Cu_4Q_9$ crystals. The elements, strontium (53.21 mg, 0.61 mmol), zirconium (36.93 mg, 0.40 mmol), copper (51.45 mg, 0.81 mmol), and sulfur (58.41 mg, 1.82 mmol) were poured in a fused silica tube, which was subsequently flame-sealed under a vacuum (*ca.* 10^{-4} Torr). The inner surface of the fused silica container (8 mm outer diameter) was carbonized before its use as the reaction vessel. A box furnace was used to heat the sealed reaction mixture.

Similarly, a vacuum-sealed tube containing the elements strontium (37.28 mg, 0.43 mmol), zirconium (25.88 mg, 0.28 mmol), copper (36.05 mg, 0.57 mmol), and selenium (100.79 mg, 1.28 mmol) was also heated in the furnace to prepare single crystals of $Sr_3Zr_2Cu_4Se_9$.

The tubes were heated in the furnace using the temperature profile described in section S1 of the ESI.† After completion of the reactions, dark reddish and black-colored melted lumps were found for the reactions targeting the sulfide and selenide, respectively. These lumps were further fractured, and a few crystals were chosen for their semiquantitative elemental energy-dispersive X-ray spectroscopic (EDX) analyses using a field-emission scanning electron microscope (FE-SEM) (Model: JSM 7610F) and an X-ray spectrometer (octane elite, EDAX Inc., USA).

Most of the red-colored crystals selected from the sulfide reaction product showed Sr : Zr : Cu : S ≈ 3 : 2 : 4 : 9, consistent with the loaded $Sr_3Zr_2Cu_4S_9$ composition (Fig. 1a). A few crystals turned out to be binary SrS (1 : 1). The crystals of $Sr_3Zr_2Cu_4Se_9$ were black in color, and their average composition was also consistent with the loaded ratio of Sr : Zr : Cu : Se ≈ 3 : 2 : 4 : 9 (Fig. 1a inset).

A few of these EDX-analyzed red and black-colored crystals were further used for structural characterization at room temperature (RT) using the single-crystal X-ray diffraction (SCXRD) method.

2.1.2 Syntheses of polycrystalline $Sr_3Zr_2Cu_4Q_9$ (Q = S, Se) samples. We have employed two methods, namely, the solid-state reaction and CS_2 methods, which are described below, to synthesize the polycrystalline $Sr_3Zr_2Cu_4Q_9$ (Q = S, Se) phases.

Solid state method. Phase pure bulk polycrystalline $Sr_3Zr_2Cu_4Q_9$ (Q = S, Se) phases were prepared by first heating

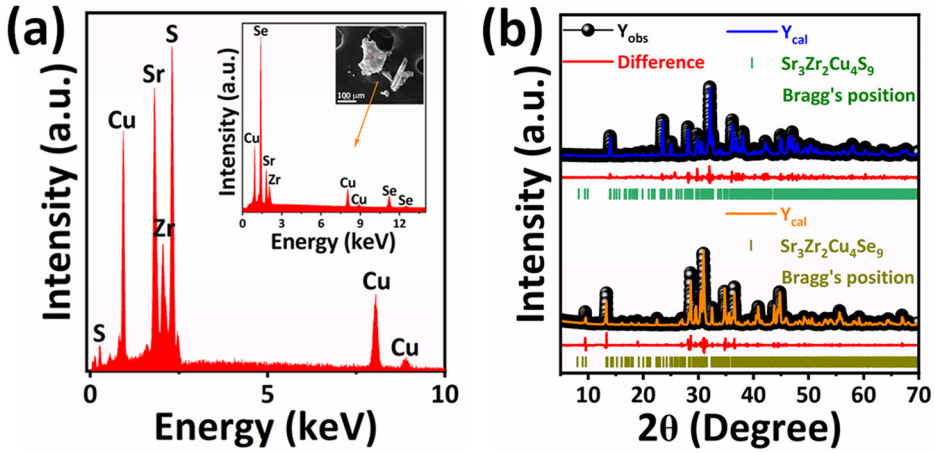

Fig. 1 (a) The EDX spectrum of a typical $Sr_3Zr_2Cu_4S_9$ crystal. The inset shows the EDX spectrum of a $Sr_3Zr_2Cu_4Se_9$ crystal. (b) The Le Bail refinement plots of the powder X-ray diffraction (PXRD) patterns of $Sr_3Zr_2Cu_4S_9$ and $Sr_3Zr_2Cu_4Se_9$.

the respective elements using the temperature profile discussed in section S1 of the ESI† and then reheating the homogenized products in the form of compressed pellets inside the vacuum-sealed fused silica tubes in two steps.

The elements, strontium (266.03 mg, 3.04 mmol), zirconium (184.65 mg, 2.02 mmol), copper (257.25 mg, 4.05 mmol), and sulfur (292.07 mg, 9.11 mmol), were sealed in a fused silica tube under vacuum and heated inside the furnace to synthesize polycrystalline $Sr_3Zr_2Cu_4S_9$.

Similarly, a vacuum-sealed fused silica tube containing strontium (186.41 mg, 2.13 mmol), zirconium (129.38 mg, 1.41 mmol), copper (180.26 mg, 2.84 mmol), and selenium (503.95 mg, 6.38 mmol) was heated in the furnace to prepare the polycrystalline $Sr_3Zr_2Cu_4Se_9$ using the heating profile discussed in section S1 of the ESI.†

The products of the reactions were homogenized into fine powders and were compressed individually into cylindrical-shaped thin pellets. These pellets were again encapsulated inside evacuated fused silica tubes and annealed at 1023 K for two days. This step is required to make high-quality polycrystalline $Sr_3Zr_2Cu_4Q_9$ (Q = S, Se) samples. The heat-treated pellets were ground again, and the products were characterized using the PXRD studies.

We also attempted to synthesize polycrystalline $Sr_3Zr_2Cu_4S_9$ by heating stoichiometric amounts of metal oxides/carbonates under N_2 and CS_2 atmosphere at 1073 K for 9 h. The details of this CS_2 method are given in section S2 of the ESI.† The ease of making bulk samples and the scalability of the method without the need for expensive fused silica tubes were the motivations behind attempting the CS_2 method. However, we failed to synthesize the phase pure material *via* the CS_2 method. Further optimization of the reaction temperature and time is required to find suitable reaction conditions to synthesize the $Sr_3Zr_2Cu_4S_9$ phase in the future.

The PXRD data sets of the powdered samples mentioned above were collected with the help of a PANalytical X'pert pro-X-ray diffractometer (Cu-$K\alpha$, λ = 1.5406 Å) at RT. The TOPAS V6 software program was used to refine the unit cell parameters of the polycrystalline samples, $Sr_3Zr_2Cu_4Q_9$, using the Le Bail refinement method (Fig. 1b).[44]

2.2 Single-crystal X-ray diffraction studies

Two SCXRD datasets for the $Sr_3Zr_2Cu_4S_9$ and $Sr_3Zr_2Cu_4Se_9$ crystals at RT under a normal atmosphere were recorded using a Bruker D8 Venture diffractometer. We used EDX-characterized crystals for the SCXRD studies. The diffractometer was fitted with a Photon III mixed-mode X-ray detector. Graphite was utilized to monochromatize the X-ray radiations from a Mo-$K\alpha$ radiation source (λ = 0.71073 Å). The intensity data for the $Sr_3Zr_2Cu_4Q_9$ (Q = S, Se) crystals were collected using a series of ω and φ scans with 0.5° frame width and 2 s per frame of the exposure time with the help of the APEX3 software.[45]

The crystal structures for the $Sr_3Zr_2Cu_4Q_9$ compounds were determined and refined in the centrosymmetric triclinic space group $P\bar{1}$ with the help of the SHELXTL[46] program suite. For the sulfide structure, all the atomic positions were easily assigned to respective elements, which resulted in the formula $Sr_3Zr_2Cu_4S_9$. However, the reliability factor values were poor: $R(F)$ = 8.87%, $R_w(F_o^2)$ = 26.72%, and the maximum positive residual electron density was 13.3 e^- $Å^{-3}$. Later, the CELLNOW[45] program was used to check the presence of any twinning in the dataset, which identified two twin domains for the crystal. Also, absorption correction was done afterward using the TWINABS.[47] The second twin domain was found to be rotated from the first domain with an angle of about 180° along the [1 0 1] direction. After these steps, the refinement parameters were significantly improved with final $R(F)$ = 4.74% and $R_w(F_o^2)$ = 12.38%. The $Sr_3Zr_2Cu_4S_9$ structure is stoichiometric and isostructural to the $Ba_3Zr_2Cu_4S_9$[48] (space group: $P\bar{1}$) structure. The final structure solution identified a total of 18 independent sites, out of which three sites were identified as Sr, two as Zr, four sites as Cu, and the remaining nine as S sites. The STRUCTURE TIDY[49] program was used to standardize the atomic positions of the $Sr_3Zr_2Cu_4Q_9$ structure.

We also found multiple twin domains for the $Sr_3Zr_2Cu_4Se_9$ dataset using the CELLNOW[45] program. Similar to the sulfide structure, for this structure as well, the two domains are related with a rotation angle of about 180° with the [1 0 1] direction as the rotation axis. The APEX3[45] was used to integrate the SCRXD dataset using two twin domains in the triclinic setting. The TWINABS[47] was used for the X-ray absorption corrections of the observed reflections. The final structure solution of the $Sr_3Zr_2Cu_4Se_9$ with the $P\bar{1}$ space group was comprised of nineteen crystallographically independent sites. The structure was refined considering 100% occupancy for all the atoms. The reliability parameters $R(F)$ and $R_w(F_o^2)$ were 6.68% and 17.56%, respectively. The anisotropic displacement parameters (ADPs) of the Cu atoms were abnormally large, indicating some vacancies at these sites. Subsequently, the fractional occupancy factor (SOF) values of these sites were allowed to be refined freely, resulting in an improvement of the reliability parameters: $R(F)$ = 5.34% and $R_w(F_o^2)$ = 11.82%. The freely refined SOF values of the Cu1, Cu3, and Cu4 atomic sites are 0.598, 0.856, and 0.533. The final refined formula, $Sr_3Zr_2Cu_{3.99(1)}Se_9$, is close to the electrically neutral composition, $Sr_3Zr_2Cu_4Se_9$. Thus, we refer to the chemical formula of the selenide as $Sr_3Zr_2Cu_4Se_9$ in this study.

We finally validated the symmetry of the $Sr_3Zr_2Cu_4S_9$ and $Sr_3Zr_2Cu_4Se_9$ structures using the ADDSYM program of the PLATON[50] software. Further crystallographic details are given in Tables 1, 2 and Tables S1, S2, S3, and S4 in the ESI.†

2.3 Solid-state ultraviolet-visible (UV-vis)-near-infrared (NIR) spectroscopy

Diffuse reflectance datasets of the polycrystalline $Sr_3Zr_2Cu_4S_9$ and $Sr_3Zr_2Cu_4Se_9$ samples were recorded at RT using a spectrophotometer JASCO V-770. A dry sample of $BaSO_4$ was used for calibration. The Kubelka–Munk equation[51] was utilized to obtain absorption data from the reflectance data.

Table 1 Crystallographic data and structure refinement details for $Sr_3Zr_2Cu_4S_9$ and $Sr_3Zr_2Cu_4Se_9$[a]

	$Sr_3Zr_2Cu_4S_9$	$Sr_3Zr_2Cu_4Se_9$
Space group	$P\bar{1}$	
a (Å)	6.6907(13)	6.9779(14)
b (Å)	10.312(2)	10.685(2)
c (Å)	11.929(2)	12.302(3)
α (°)	109.49(3)	109.18(3)
β (°)	104.54(3)	105.38(3)
γ (°)	96.73(3)	96.56(3)
V (Å^3)	732.6(3)	814.6(3)
Z	2	
ρ (g cm^{-3})	4.479	5.745
μ (mm^{-1})	19.12	36.13
$R(F)$[b]	0.047	0.053
$R_w(F_o^2)$[c]	0.124	0.118

[a] λ = 0.71073 Å, T = 298(2) K. [b] $R(F) = \sum||F_o| - |F_c||/\sum|F_o|$ for $F_o^2 > 2\sigma(F_o^2)$. [c] $R_w(F_o^2) = \{\sum[w(F_o^2 - F_c^2)^2]/\sum wF_o^4\}^{1/2}$. For $F_o^2 < 0$, $w = 1/[\sigma^2(F_o^2) + (mP)^2 + nP]$; where $P = (F_o^2 + 2F_c^2)/3$. For the sulfide structure, m = 0.0574 and n = 6.3137, and for the selenide structure, m = 0 and n = 27.2292.

Table 2 Important bond distances (in Å) of the $Sr_3Zr_2Cu_4Q_9$ structures

	$Sr_3Zr_2Cu_4S_9$	$Sr_3Zr_2Cu_4Se_9$
Zr–Q (Å)	2.490(2)–2.694(2)	2.6342(19)–2.8083(18)
Tetrahedral Cu–Q (Å)	2.309(2)–2.372(2)	2.386(4)–2.682(5)
Trigonal Cu–Q (Å)	2.234(2)–2.312(2)	—
Sr–Q (Å)	2.924(3)–3.628(2)	3.0655(19)–3.4277(19)

2.4 Thermal conductivity (κ_{tot}) measurements

$Sr_3Zr_2Cu_4S_9$ and $Sr_3Zr_2Cu_4Se_9$ powders were first pressed into thin cylindrical pellets (dia. 8 mm) and then sintered at 973 K (for 24 h) using the sealed tube method. A hydraulic press was used to compact the powders into hard pellets under *ca.* 8 tons of pressure. The density (d) values of the resulting compact pellets of $Sr_3Zr_2Cu_4S_9$ and $Sr_3Zr_2Cu_4Se_9$ were determined using the Archimedes method.[52] The experimental density values were about 92% of the theoretical density.

The thermal diffusivity (D) values of $Sr_3Zr_2Cu_4S_9$ and $Sr_3Zr_2Cu_4Se_9$ were measured using a LINSEIS XFA 500 instrument. The details of the measurements are given elsewhere.[41] The Dulong–Petit law[53] was employed to estimate the heat capacity (C_p) values of the $Sr_3Zr_2Cu_4S_9$ and $Sr_3Zr_2Cu_4Se_9$ samples. Finally, the total thermal conductivity ($\kappa_{tot} = D \times d \times C_p$) values were calculated. The final κ_{tot} value has an uncertainty of around ±10%.

2.5 Transport property measurements for $Sr_3Zr_2Cu_4S_9$ and $Sr_3Zr_2Cu_4Se_9$

The sintered rectangular parallelepiped-shaped $Sr_3Zr_2Cu_4S_9$ and $Sr_3Zr_2Cu_4Se_9$ pellets were obtained using the method described in section 2.4. The electrical resistivity (ρ) values of the $Sr_3Zr_2Cu_4Q_9$ (Q = S, Se) pellets were measured at low temperatures using the standard four-contact method. The pellets were cooled using a Janis SHI-950 closed-cycle cryostat, and the four contacts on each of the pellets were made using the Cu-probes (0.05 mm diameter) and Ag-paint. A nanovoltmeter (Keithley, Model: 2182A) and a current source (Keithley, Model: 6221) were used for the study.

The $Sr_3Zr_2Cu_4Se_9$ pellet was further used for the simultaneous determination of electrical resistivity and Seebeck coefficient (S) values at higher temperatures (323 K–573 K) with the help of a ULVAC-RIKO ZEM-3 equipment under a low-pressure He-atmosphere. No hysteresis between the heating and cooling cycles of the measured data was observed.

2.6. Photovoltaic study of $Sr_3Zr_2Cu_4S_9$

A photoanode, FTO/TiO_2/CdS, was prepared using the method described elsewhere.[38] The powdered $Sr_3Zr_2Cu_4S_9$ was dispersed in toluene at 1 mg mL^{-1} concentration by ultrasonication for 2 h and then drop-casted over the FTO/TiO_2/CdS electrode and dried under vacuum for two days to obtain a FTO/TiO_2/CdS/$Sr_3Zr_2Cu_4S_9$ photoanode.

A counter electrode (CE) was fabricated by coating MWCNTs over a Ni foam substrate. CB, PVdF, and MWCNTs were mixed in a 1 : 1 : 8 weight ratio, ground well, and con-

verted into a slurry using NMP. The slurry was coated on the Ni-foam and dried. A polysulfide gel was prepared by adding 5 wt% of fumed silica in an aqueous suspension of (1 M Na_2S + 1 M S) under constant stirring until it became a uniform gel.

Finally, we made the solar cells, FTO/TiO_2/CdS/S^{2-}, S/MWCNTs/Ni-foam and FTO/TiO_2/CdS/$Sr_3Zr_2Cu_4S_9$/S^{2-}, and S/MWCNTs/Ni-foam, by sandwiching the polysulfide gel in between the photoanodes and the CE using binder clips. These solar cells were subjected to *I–V* measurements with the help of a Newport Oriel 3A solar simulator coupled with a Keithley 2420 source meter. A 450 W Xenon arc lamp was used as the light source with a light intensity of 100 mW cm^{-2} and Air Mass (AM) 1.5G illumination; the spatial uniformity of irradiance was determined by calibrating with a 2 cm × 2 cm Si reference cell and confirmed using a Newport power meter.

2.7 Theoretical and computational methodologies

We employed density functional (DFT) calculations[54] to investigate the electronic structures and estimate the structural parameters of relaxed $Sr_3Zr_2Cu_4S_9$ and $Sr_3Zr_2Cu_4Se_9$ unit cells. The Kohn–Sham equations within the DFT framework are solved using the plane wave basis expansion with the help of the VASP package.[55] Further details of the theoretical calculations are given in the ESI (see Section S3).† We used the $Sr_3Zr_2Cu_4Se_9$ unit cell with half-occupied (50%) Cu1 and Cu4 atomic sites for the calculations.

3. Results and discussion

3.1 Syntheses

The $Sr_3Zr_2Cu_4S_9$ and $Sr_3Zr_2Cu_4Se_9$ crystals were prepared by the reaction of elements at high temperatures (T_{max} = 1223 K) and slow cooling of the reaction mixtures to RT. The $Sr_3Zr_2Cu_4S_9$ crystals were red in contrast to the black-colored crystals of the $Sr_3Zr_2Cu_4Se_9$ phase.

Furthermore, we used two methods to prepare bulk polycrystalline samples of $Sr_3Zr_2Cu_4S_9$: (a) the direct reaction of elements at high temperatures and (b) the CS_2 method. The CS_2 method failed to produce the targeted $Sr_3Zr_2Cu_4S_9$ phase. Instead, the cubic SrS phase (space group: $Fm\bar{3}m$)[56] was formed as the major phase according to the PXRD analysis (see Fig. S1 of the ESI†). Presumably, the phases containing Zr and Cu are amorphous in the powdered sample obtained by the CS_2 reaction. On the other hand, the high-temperature reaction of elements with one intermittent grinding and reheating produced a monophasic $Sr_3Zr_2Cu_4S_9$ sample. The polycrystalline $Sr_3Zr_2Cu_4Se_9$ sample was prepared using heating conditions similar to those employed for the sulfide sample.

The PXRD patterns of the $Sr_3Zr_2Cu_4Q_9$ (Q = S, Se) phases are shown in Fig. 1b. The refined unit cell parameters of $Sr_3Zr_2Cu_4S_9$ and $Sr_3Zr_2Cu_4Se_9$, calculated from the PXRD data using the Le Bail refinement method, are a = 6.695(2) Å, b = 10.322(1) Å, c = 11.941(2) Å, α = 109.60(1)°, β = 104.54(1)°, γ = 96.67(1)°, and a = 6.986(2) Å, b = 10.695(2) Å, c = 12.272(1) Å, α = 109.33(1)°, β = 105.35(1)°, γ = 96.57(1)°, respectively. The cell parameters of $Sr_3Zr_2Cu_4Q_9$ (Q = S, Se) obtained from the powder and single crystal XRD studies are in good agreement.

3.2 Crystal structure description

The quaternary sulfide $Sr_3Zr_2Cu_4S_9$ is the first quaternary compound found in the Sr–Zr–Cu–S system, whereas $Sr_3Zr_2Cu_4Se_9$ is the second member of the Sr–Zr–Cu–Se system for which a Sr-deficient phase $Sr_{0.5}ZrCuSe_3$ [43] is known in the literature.

The single-crystal XRD study showed that, at RT, $Sr_3Zr_2Cu_4S_9$ crystallizes in the triclinic $Ba_3Zr_2Cu_4S_9$ [48] structure. As expected, the unit cell volume of the centrosymmetric triclinic $Sr_3Zr_2Cu_4S_9$ structure (space group: $P\bar{1}$) with the refined cell parameters a = 6.6907(13) Å, b = 10.312(2) Å, c = 11.929(2) Å, α = 109.49(3)°, β = 104.54(3)°, and γ = 96.73(3)°, is smaller than the $Ba_3Zr_2Cu_4S_9$ cell. These experimental lattice parameters augur well with those obtained from theoretical calculations (see section 3.7). The asymmetric unit of the $Sr_3Zr_2Cu_4S_9$ structure contains nine sulfur and nine metal sites (3 × Sr sites, 2 × Zr sites, and 4 × Cu sites). As seen in Fig. 2a, the $^{\infty}_{2}[Zr_2Cu_4S_9]^{6-}$ layers of the $Sr_3Zr_2Cu_4S_9$ structure are separated by the Sr^{2+} cations. The anionic $^{\infty}_{2}[Zr_2Cu_4S_9]^{6-}$ layer features distorted ZrS_6 octahedra, CuS_4 tetrahedra (Cu2 and Cu4), and trigonal planar CuS_3 units (Cu1 and Cu3), which serve as the main motifs of the structure.

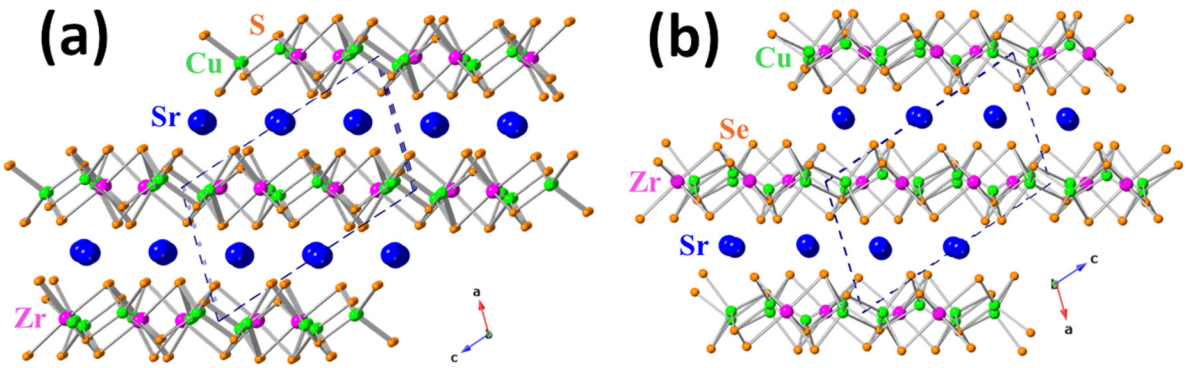

Fig. 2 The unit cells of (a) $Sr_3Zr_2Cu_4S_9$ and (b) $Sr_3Zr_2Cu_4Se_9$ crystal structures along the *b*-axis.

The $Sr_3Zr_2Cu_4Se_9$ structure is isoelectronic to the related sulfide. Interestingly, its structure is different from the $Sr_3Zr_2Cu_4S_9$ structure. The selenide adopts the original structure type with triclinic symmetry (space group: $P\bar{1}$). The refined cell constants of the $Sr_3Zr_2Cu_4Se_9$ structure are a = 6.9779(14) Å, b = 10.685(2) Å, c = 12.302(3) Å, α = 109.18(3)°, β = 105.38 (3)°, and γ = 96.56(3)°. In contrast to the sulfide structure, the $Sr_3Zr_2Cu_4Se_9$ phase is non-stoichiometric with partially vacant Cu sites. $Sr_3Zr_2Cu_4Se_9$ is best described as the pseudo-2D structure, like the sulfide structure, as shown in Fig. 2b.

The selenide structure comprises nineteen independent atoms (3 × Sr, 2 × Zr sites, 5 × Cu sites, and 9 × Se sites), *i.e.*, one additional Cu site in reference to the sulfide structure. The three Cu sites, Cu1, Cu3, and Cu4, have free SOF values of 0.598(8), 0.856(7), and 0.532(8), respectively, in the $Sr_3Zr_2Cu_4Se_9$ structure. The composition of the infinite layers present in the selenide structure is identical to the sulfide structure, *i.e.*, $^{\infty}_{2}[Zr_2Cu_4Se_9]^{6-}$ and their negative charges are counterbalanced by the Sr^{2+} ions. The Zr and Cu atoms in the selenide structure are octahedrally and tetrahedrally coordinated with the Se atoms, respectively. The short Cu1···Cu1 and Cu4···Cu4 distances (<2.2 Å) in the $Sr_3Zr_2Cu_4Se_9$ structure are the result of their occupancy disorder and imply that these Cu atoms do not coexist simultaneously close to each other in the structure.

Next, we compare the layers of the $Sr_3Zr_2Cu_4S_9$ and $Sr_3Zr_2Cu_4Se_9$ structures in Fig. 3.

The layers of both the structures have edge and vertex-sharing ZrQ_6 octahedra (see Fig. 3). The oppositely oriented $Cu2S_4$ and $Cu4S_4$ tetrahedra share edges and vertices with the ZrS_6 octahedra to form chains of $^{\infty}_{1}[Zr_2Cu_2S_9]^{8-}$ (see Fig. 3a). Similarly, the connectivity of $ZrSe_6$ octahedra, $Cu2Se_4$, and $Cu5Se_4$ tetrahedra in the $Sr_3Zr_2Cu_4Se_9$ structure creates $^{\infty}_{1}[Zr_2Cu_2Se_9]^{8-}$ chains (see Fig. 3b). Finally, the $^{\infty}_{2}[Zr_2Cu_4Q_9]^{6-}$ layers in both structures are formed by filling of Cu atoms in the structures, which hold together the $^{\infty}_{1}[Zr_2Cu_2Q_9]^{8-}$ chains, as shown in Fig. 3. The main difference between the layers of the title structures is the bonding environments of the additional Cu atoms, Cu1 and Cu3, of the sulfide structure and Cu1, Cu3, and Cu4 atoms in the selenide structure. The Cu atoms (Cu1 and Cu3) in the sulfide structure are only three-coordinated in contrast to the four-coordinated (tetrahedral) Cu atoms of the selenide structure.

The important interatomic distances of the $Sr_3Zr_2Cu_4Q_9$ structures are provided in Table 2. The Zr–S distances of $Sr_3Zr_2Cu_4S_9$ (see Table 2) match well with the corresponding distance of the $Ba_3Zr_2Cu_4S_9$ (2.525(1) Å–2.704(1) Å)[48] structure. The Cu–S distances of the CuS_3 unit (2.234(2) Å–2.312(2) Å) are shorter than the tetrahedral CuS_4 units (2.309(2) Å–2.372(2) Å) in the title sulfide structure. These distances compare well with those found in $Ba_3Zr_2Cu_4S_9$ (2.241(2) Å–2.364(2) Å)[48] and the $BaCeCuS_3$ (2.351(1) Å–2.461(2) Å)[38] structures.

The Cu–Se (2.386(4) Å–2.682(5) Å) distances of $Sr_3Zr_2Cu_4Se_9$ are consistent with those found in the $BaCu_2Se_2$ (2.456(1) Å to 2.618(3) Å)[57] and $BaNdCuSe_3$ (2.460(4) Å to 2.567(3) Å)[58] structures. The Zr–Se bond distances of $ZrSe_6$ octahedra vary from 2.6342(19) Å to 2.8083(18) Å in the $Sr_3Zr_2Cu_4Se_9$ structure. These distances are in good agreement with those reported for the $Ba_{0.5}ZrCuSe_3$ (2.661(7) Å to 2.707(5) Å)[43] and $Ba_8Zr_2Se_{11}(Se_2)$ (2.6337(7) Å to 2.7940(7) Å)[42] structures.

Another interesting feature of $Sr_3Zr_2Cu_4Q_9$ (Q = S, Se) is the Cu···Cu interactions, which are intermediate to the single Cu–Cu bond (~2.556 Å)[59] and the van der Waals distance of 2.80 Å (ref. 60) between two Cu atoms. These interactions are shown in Fig. 4 for the $Sr_3Zr_2Cu_4Q_9$ (Q = S, Se) structures. The Cu···Cu interactions are shorter in the $Sr_3Zr_2Cu_4Se_9$ structure (2.621(5) Å to 2.711(4) Å) than in the $Sr_3Zr_2Cu_4S_9$ structure (2.753(3) Å to 2.845(3) Å). Similar Cu···Cu interactions are also known for the Cu_5FeS_4 (2.587 Å–2.989 Å),[61] $K_2Cu_3AlS_4$ (2.734(3) Å–2.736(3) Å),[62] and Cu_3SbSe_3 (2.665(2) Å)[63] structures. The chalcogen atoms of $Sr_3Zr_2Cu_4Q_9$ structures make distorted bicapped trigonal prism-like geometries around the Sr atoms, as shown in Fig. S2 in the ESI.†

To the best of our knowledge, only monovalent copper species are known for the chalcogenide structures. Also, the $Sr_3Zr_2Cu_4Q_9$ structures are traditional chalcogenides (not polychalcogenides) with more stable Q^{2-} species. Therefore, these two structures can be charge balanced with the Sr^{2+}, Zr^{4+},

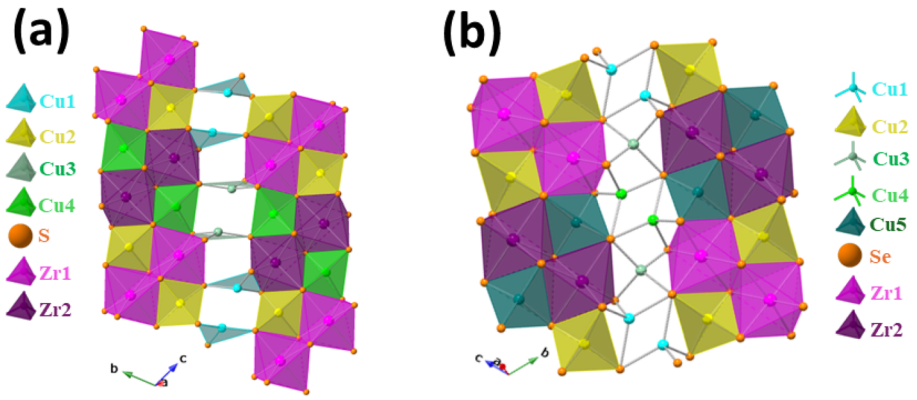

Fig. 3 (a) The $^{\infty}_{1}[Zr_2Cu_2S_9]^{8-}$ chains that are bridged by the Cu1 and Cu3 atoms in the $Sr_3Zr_2Cu_4S_9$ and (b) $^{\infty}_{1}[Zr_2Cu_2Se_9]^{8-}$ chains of the $Sr_3Zr_2Cu_4Se_9$ that are bridged by the Cu1, Cu3, and Cu4 atoms to form infinite layers of $^{\infty}_{2}[Zr_2Cu_4Se_9]^{6-}$.

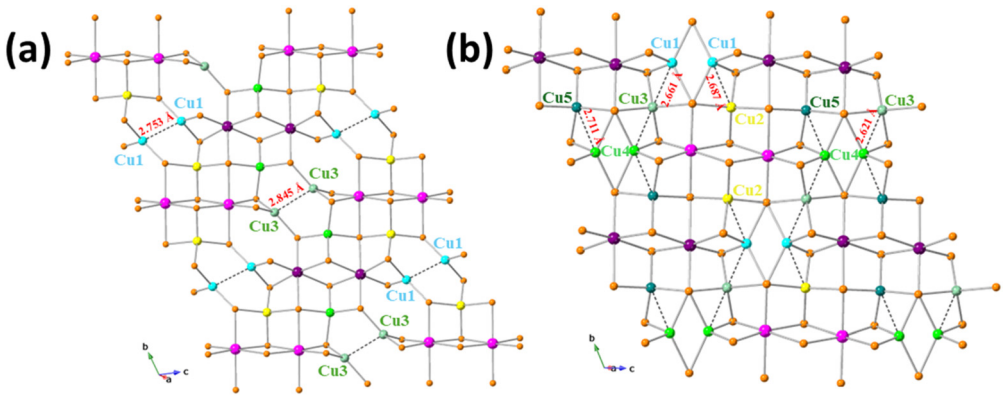

Fig. 4 A fragment of the $^{\infty}_{2}[Zr_2Cu_4Q_9]^{6-}$ layers showing the short Cu···Cu interactions in (a) $Sr_3Zr_2Cu_4S_9$ and (b) $Sr_3Zr_2Cu_4Se_9$ structures.

Cu^{1+}, and Q^{2-} species, *i.e.*, the charge partitioned formula of the title phases is $(Sr^{2+})_3(Zr^{4+})_2(Cu^{1+})_4(Q^{2-})_9$.

3.3 Structural relationship between $Ak_3Zr_2Cu_4S_9$ (*Ak* = Ba and Sr), $Sr_3Zr_2Cu_4Se_9$, and $Sr_{0.5}ZrCuSe_3$ structures

We next correlate the structural aspects of the three structure types: $Ak_3Zr_2Cu_4S_9$ (*Ak* = Ba and Sr),[48] $Sr_3Zr_2Cu_4Se_9$, and $Sr_{0.5}ZrCuSe_3$ [43] structures. A common feature of these structure types is the presence of anionic layers built up of the transition metals and *Q* (S/Se) atoms. These anionic frameworks are counterbalanced and separated by the Ak^{2+} cations (*Ak* = Ba and Sr) (see Fig. 5). Among these structures, $Sr_{0.5}ZrCuSe_3$ [43] is stabilized with the highest symmetry (space group: *Cmcm*) and is isotypic with the $KCuZrS_3$ (*Cmcm*)[64] structure type. In the literature, a large number of quaternary chalcogenides are known to adopt the $KCuZrS_3$ [64] type structure.

The $Sr_3Zr_2Cu_4Se_9$ ($P\bar{1}$) type is closely related to $Sr_{0.5}ZrCuSe_3$ [43] in terms of the coordination environments of the transition metals, *i.e.*, Zr and Cu atoms, which occupy distorted octahedral and tetrahedral sites, respectively. The CuS_3 units with a triangular planar geometry make the triclinic $Ak_3Zr_2Cu_4S_9$ (*Ak* = Ba and Sr) structure type ($P\bar{1}$)[48] unique to the other two structure types. No short Cu···Cu interactions exist in the $Sr_{0.5}ZrCuSe_3$ [43] structure. In contrast, the $Ak_3Zr_2Cu_4S_9$ (*Ak* = Ba and Sr) and $Sr_3Zr_2Cu_4Se_9$ structure types feature a variety of short Cu···Cu interactions.

Although the $Ak_3Zr_2Cu_4S_9$ (*Ak* = Ba, Sr) and $Sr_3Zr_2Cu_4Se_9$ structures are isoelectronic and layered, the intralayer connections are entirely different in these two structure types, as described above (see Fig. 3). While the stoichiometric sulfur compound has two Cu sites as the bridging elements, the non-stoichiometric selenide compound has three Cu atoms to link the $^{\infty}_{1}[Zr_2Cu_2Q_9]^{8-}$ chains, as shown in Fig. 3 and 4. Thus, the flexibility of copper atoms to stabilize different polyhedra in the title sulfide structure can be considered as the main contrasting feature between the $Ak_3Zr_2Cu_4S_9$ and $Sr_3Zr_2Cu_4Se_9$ types.

3.4 Optical bandgap and electrical resistivity

We used the polycrystalline samples of $Sr_3Zr_2Cu_4Q_9$ (*Q* = S, Se) for physical property measurements. The Tauc plot of the $Sr_3Zr_2Cu_4S_9$ powder shows a sharp drop in absorption coefficient (α) value below 2 eV, as shown in Fig. 6a.

A direct bandgap energy value of 1.7(1) eV is calculated for the $Sr_3Zr_2Cu_4S_9$ phase from the Tauc plot, which agrees with the reddish-brown color of the powder. The theoretical bandgap of 1.78 eV for the $Sr_3Zr_2Cu_4S_9$ structure is in good

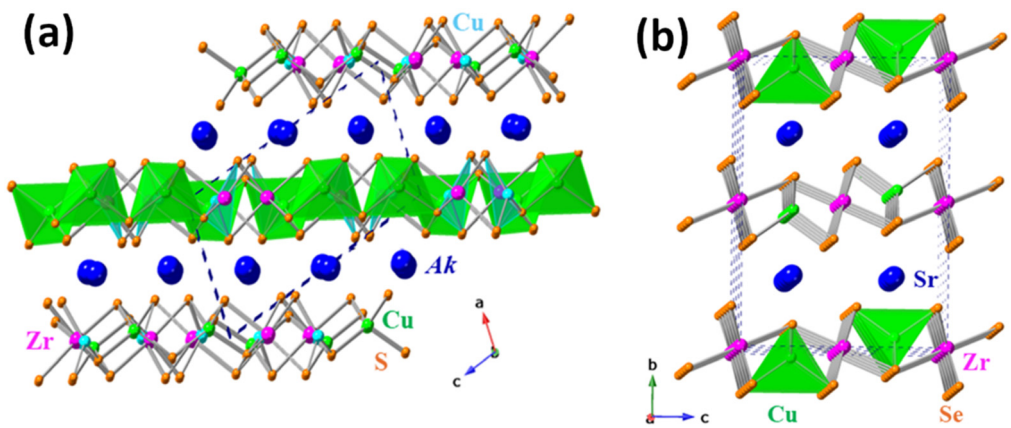

Fig. 5 Unit cells of the (a) $Ak_3Zr_2Cu_4S_9$ (*Ak* = Ba, Sr) ($P\bar{1}$) and (b) $Sr_{0.5}ZrCuSe_3$ (*Cmcm*) structures.

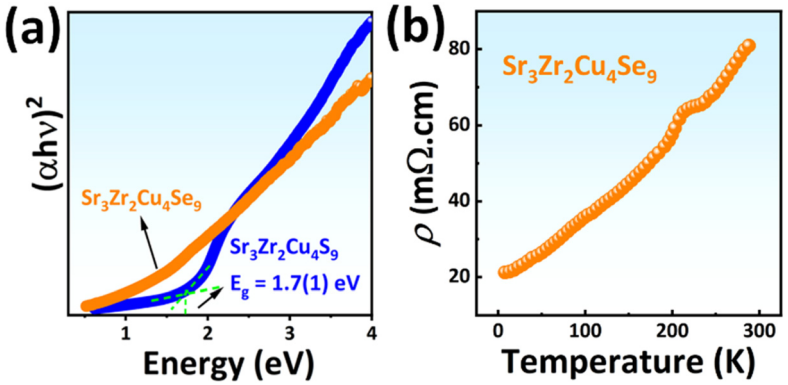

Fig. 6 (a) Tauc plots of the finely ground polycrystalline $Sr_3Zr_2Cu_4S_9$ and $Sr_3Zr_2Cu_4Se_9$ samples. (b) The electrical resistivity plot of the $Sr_3Zr_2Cu_4Se_9$ compound below RT.

agreement with the experimental value (see section 3.7 for details). On the other hand, $Sr_3Zr_2Cu_4Se_9$, which is black in color, does not show any sharp transition in the Tauc plot, indicating that this selenide has a narrow bandgap energy (E_g < 0.6 eV), or it is a metal/semimetal.

The sulfide sample, $Sr_3Zr_2Cu_4S_9$, is electrically insulating, having resistance values of the order of MΩ at RT in contrast to the $Sr_3Zr_2Cu_4Se_9$, which has electrical resistivity (ρ) values of about 80 mΩ cm (at RT). The ρ-value further drops to ~20 mΩ cm on cooling the $Sr_3Zr_2Cu_4Se_9$ sample to 3 K, as shown in Fig. 6b. A kink in the resistivity plot was observed at ~225 K, and this effect was reproducible. The origin of the kink observed in the resistivity plot is not clear. The resistivity values of $Sr_3Zr_2Cu_4Se_9$ are several orders higher than coinage metals like Cu (1.7×10^{-3} mΩ cm at RT) and Ag (1.6×10^{-3} mΩ cm at RT). Thus, $Sr_3Zr_2Cu_4Se_9$ can be described as a poor metal or a degenerate semiconductor. The detailed theoretical electronic structure of $Sr_3Zr_2Cu_4Se_9$ is discussed in section 3.7.

3.5 High-temperature transport studies: thermal conductivity (κ_{tot}), Seebeck coefficient (S), and electrical resistivity (ρ)

Both $Sr_3Zr_2Cu_4S_9$ and $Sr_3Zr_2Cu_4Se_9$ are relatively good heat conductors in comparison to related layered quaternary structures such as the $RbZrCuTe_3$ (0.49 W mK^{-1} at 323 K to 0.35 W mK^{-1} at 575 K)[31] and $BaCeCuS_3$ (0.62 W mK^{-1} at 323 K to 0.32 W mK^{-1} at 773 K).[38] The $Sr_3Zr_2Cu_4Se_9$ compound shows a κ_{tot} of 3.5 W mK^{-1} at 323 K, which is almost twice the value observed for $Sr_3Zr_2Cu_4S_9$ (1.82 W mK^{-1} at 323 K). As expected, the κ_{tot} values gradually decreased as the samples were heated from 323 K to higher temperatures (573 K). The κ_{tot} value drops to 2.5 W mK^{-1} and 1.4 W mK^{-1} for $Sr_3Zr_2Cu_4Se_9$ and $Sr_3Zr_2Cu_4S_9$, respectively, at 573 K (Fig. 7a).

The κ_{tot} value for each sample is the sum of the electronic (κ_{ele}) and lattice thermal conductivities (κ_{lat}) of the crystals. Since $Sr_3Zr_2Cu_4Se_9$ is metallic, in contrast to the insulating $Sr_3Zr_2Cu_4S_9$, the free charge carriers in the former compound contribute to the total thermal conductivity. On the contrary, the κ_{ele} value of the insulating $Sr_3Zr_2Cu_4S_9$ is negligible in comparison to the κ_{lat} values. We calculated the κ_{ele} value of $Sr_3Zr_2Cu_4Se_9$ using the Wiedemann–Franz model[65] (refer to the caption of Fig. S3 in the ESI†) to compare the κ_{lat} values of the two compounds. The κ_{lat} value is also higher for $Sr_3Zr_2Cu_4Se_9$ (3.08 W mK^{-1} to 2.1 W mK^{-1} in the range of 323 K to 573 K) than for the isoelectronic sulfide (see Fig. 7a). The higher thermal conductivity values for $Sr_3Zr_2Cu_4Q_9$ (Q = S, Se) make them unsuitable for thermoelectric applications.

Next, we discuss the trends of the Seebeck coefficient and resistivity data obtained for $Sr_3Zr_2Cu_4Se_9$ as a function of

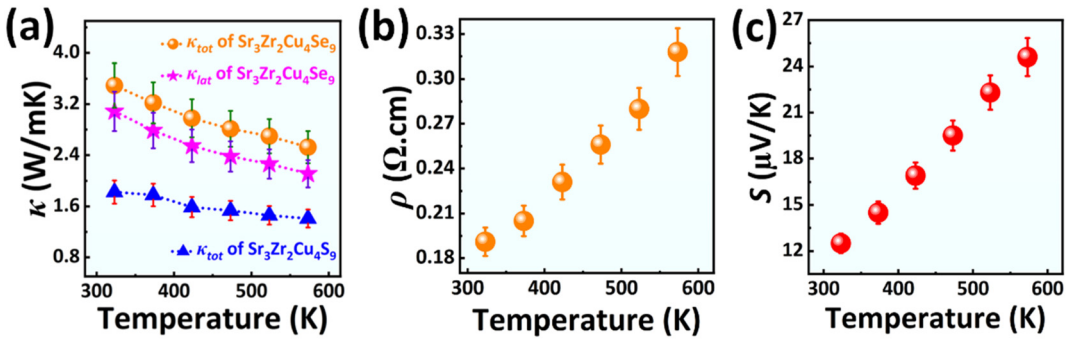

Fig. 7 (a) Temperature-dependent thermal conductivity plots of $Sr_3Zr_2Cu_4Q_9$ (Q = S, Se) compounds. (b) Electrical resistivity and (c) Seebeck coefficient as a function of temperature for the $Sr_3Zr_2Cu_4Se_9$ compound.

temperature. The electrical resistivity plot shown in Fig. 7b is consistent with metal-like behavior with a gradual increase in ρ-values on increasing the sample's temperature. The ρ-value of $Sr_3Zr_2Cu_4Se_9$ elevated from 190 mΩ cm at 323 K to 320 mΩ cm at 573 K. The *p*-type nature of $Sr_3Zr_2Cu_4Se_9$ is confirmed by the positive sign of the *S*-values, as shown in Fig. 7c. As expected, the *S*-value increases at higher temperatures as the sample becomes more electrically resistive. Unfortunately, the low *S* values (12.51 μV K^{-1} at 323 K to 24.60 μV K^{-1} at 573 K) combined with the relatively higher thermal conductivity values of the $Sr_3Zr_2Cu_4Se_9$ sample make it unsuitable for thermoelectric applications.

The maximum thermoelectric figure of merit, *z*T, is almost zero (16.5×10^{-7}), as can be seen from the *z*T plot in Fig. S3 in the ESI.† Further improvement of the *z*T value by optimization of the charge carrier concentration seems unlikely due to the poor *S*-value of $Sr_3Zr_2Cu_4Se_9$.

3.6 Photovoltaic studies of the $Sr_3Zr_2Cu_4S_9$ polycrystalline compound

The current density (J)–voltage (V) measurements of the solar cells were performed under one sun illumination. The J–V plot of the solar cell, FTO/TiO_2/CdS/S^{2-}, S/MWCNTs/Ni-foam, presented in Fig. 8, shows the open circuit voltage (V_{OC}) = 723 mV, short circuit current density (J_{SC}) = 13.00 mA cm^{-2}, fill factor (FF) = 58.83%, and the power conversion efficiency (PCE or η) = 5.59%.

The J–V plot of the FTO/TiO_2/CdS/$Sr_3Zr_2Cu_4S_9$/S^{2-}, S/MWCNTs/Ni-foam shows: V_{OC} = 868 mV, J_{SC} = 13.28 mA cm^{-2}, FF = 60.11%, and the efficiency = 6.93%, as seen in Table 3. From the Tauc plot, shown in Fig. 6a, the bandgap of $Sr_3Zr_2Cu_4S_9$ was estimated to be 1.7 eV, which is much lower than the bandgaps of TiO_2 (3.2 eV) and CdS (2.3 eV) used in our solar cell. By the inclusion of $Sr_3Zr_2Cu_4S_9$ in the photoanode, the overall efficiency was increased by ~24% because $Sr_3Zr_2Cu_4S_9$, a narrow band gap semiconductor, serves as a co-sensitizer. This implies that in the co-sensitized cell, upon illumination, in addition to the CdS, the $Sr_3Zr_2Cu_4S_9$ phase also undergoes an electron–hole separation. Hence, in the co-sensitized cell, additional charge carriers are available for circulation, improving the V_{OC} as well as the J_{SC}, thus increasing the efficiency of the cell. Furthermore, co-sensitization also reduces back electron transfer to the electrolyte during cell operation, which maximizes charge separation and enhances efficiency.

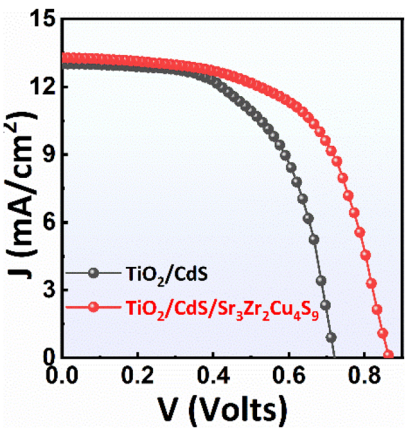

Fig. 8 The *J*–*V* characteristics of the solar cells based on different photoanodes, S^{2-}, S gel electrolyte, and MWCNTs/Ni-foam as CE under 1 sun (AM 1.5G, 100 m cm^{-2}).

Table 3 Parameters of the solar cells containing 1 M polysulfide gel electrolyte and MWCNTs/Ni-foam as CE, under 1 sun illumination (AM 1.5G, 100 mW cm^{-2}) and with an exposed cell area of ~0.1 cm^2

Photoanode	V_{OC} (mV)	J_{SC} (mA cm^{-2})	FF (%)	PCE (%)
FTO/TiO_2/CdS	723	13.00	58.83	5.59
FTO/TiO_2/CdS/$Sr_3Zr_2Cu_4S_9$	868	13.28	60.11	6.93

3.7 Band structures of $Sr_3Zr_2Cu_4S_9$ and $Sr_3Zr_2Cu_4Se_9$

We estimated the structural parameters of the optimized unit cells and explored the electronic structures of $Sr_3Zr_2Cu_4S_9$ and $Sr_3Zr_2Cu_4Se_9$. The results are tabulated in Table 4 and are found to be aligned with the experimental values. As can be seen, the GGA (LDA) schemes slightly overestimate (underestimate) the cell parameters as expected. In general, the GGA (LDA) XC schemes slightly overestimate (underestimate) the cell parameters, respectively, for most of the material systems.[66] The GGA bandgap energy for $Sr_3Zr_2Cu_4S_9$ is computed to be 1.37 eV. As expected, the computed GGA bandgap value for the sulfide is lower as compared to the experimental value of ~1.7 eV since the GGA (LDA) schemes are known to underestimate the bandgaps as much as by ~50%. The bandgap of 1.78 eV for $Sr_3Zr_2Cu_4S_9$ computed using the GGA-1/2 scheme is in better agreement with the experimental value. The GGA-1/2 scheme is expected to provide better bandgap estimates since it partially corrects the self-interaction error in local and semi-local XC functionals for extended systems.

The GGA and GGA-1/2 computed bandgap values of $Sr_3Zr_2Cu_4Se_9$ are 1.17 eV and 1.56 eV, respectively. These computed bandgap energies disagree with the experimental result that suggests $Sr_3Zr_2Cu_4Se_9$ is metallic/degenerate semiconducting in nature. This disagreement may be partially attributed to the slightly different occupancy values of Cu1, Cu3, and Cu4 sites in the unit cell used to model the $Sr_3Zr_2Cu_4Se_9$ structure as compared to the experimental unit cell content obtained from the SCXRD study. In our theoretical model, the Cu1 and Cu4 sites are half occupied (50%), whereas the Cu3 site is fully occupied (100%). However, in the experimental unit cell, the Cu1, Cu3, and Cu4 sites have occupancies of 59.8%, 85.8%, and 53.3%, respectively.

Fig. 9 shows the density of states (DOS) and the band structure plots for $Sr_3Zr_2Cu_4S_9$. The energies in the DOS plot are scaled in such a way that the valence band maximum (VBM) lies at 0 (see Fig. 9a). As can be seen, the top of the valence band (VB) (~−5.5 eV < *E* < 0) is primarily comprised of Cu-3d, Zr-4d, and S-3p states. The VB at ~−12 eV is mainly contribu-

Table 4 The computed lattice parameters and bandgap (eV) values of $Sr_3Zr_2Cu_4S_9$ and $Sr_3Zr_2Cu_4Se_9$

			a (Å)	b (Å)	c (Å)	α	β	γ	E_g (eV)
$Sr_3Zr_2Cu_4S_9$	Cal.	GGA	6.719	10.321	11.937	109.41	104.79	96.80	1.37
		LDA	6.539	9.953	11.713	109.97	104.21	96.99	1.29
		GGA-1/2	—	—	—	—	—	—	1.78
	Exp.		6.662	10.232	11.939	109.69	104.84	96.39	1.7(1)
$Sr_3Zr_2Cu_4Se_9$	Cal.	GGA	7.044	10.697	12.333	109.31	105.68	96.50	1.17
		LDA	6.830	10.402	12.006	109.33	105.60	96.56	1.09
		GGA-1/2	—	—	—	—	—	—	1.56
	Exp		6.9779	10.685	12.302	109.18	105.38	96.56	0

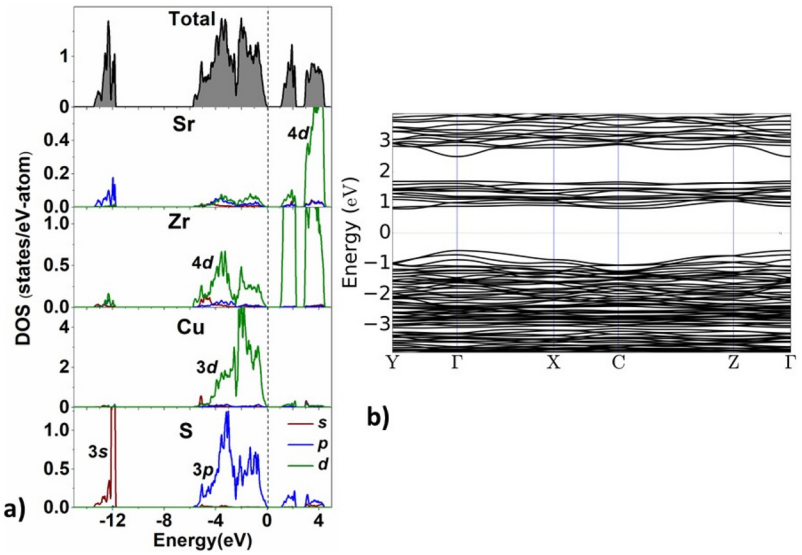

Fig. 9 (a) The total and projected density of states (DOS) and (b) the band structure plot along high symmetry directions in the Brillouin zone for $Sr_3Zr_2Cu_4S_9$. The high symmetry k-points are $Y \equiv (0, \frac{1}{2}, 0)$, $\Gamma \equiv (0, 0, 0)$, $X \equiv (\frac{1}{2}, 0, 0)$, $C \equiv (\frac{1}{2}, \frac{1}{2}, 0)$, and $Z \equiv (0, 0, \frac{1}{2})$.

ted by the S-3s localized states, with some minor contributions from the Sr-4s states. The conduction band (CB) close to the Fermi energy (~1.1 eV < E < 2.2 eV) is primarily made up of the antibonding Zr-4d states. The contributions to the CB in the higher energy range (2.9 eV < E < 4.5 eV) are from the Zr-4d and Sr-4d states. The band structure of $Sr_3Zr_2Cu_4S_9$, as shown

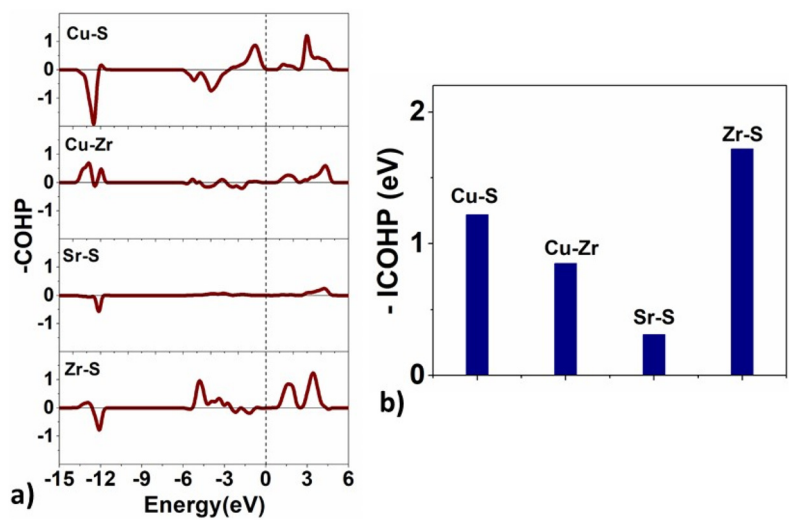

Fig. 10 (a) The crystal orbital Hamilton populations (COHP) and (b) the integrated COHP (ICOHP) values for the bonding atoms in $Sr_3Zr_2Cu_4S_9$.

in Fig. 9b, indicates that the bandgap is indirect. However, the difference between the indirect and direct bandgap is minute (~0.07 eV). The DOS and band structure plots for $Sr_3Zr_2Cu_4Se_9$ are found to be qualitatively similar to that for $Sr_3Zr_2Cu_4S_9$, as shown in Fig. S4 of the ESI.†

The projected crystal orbital Hamilton populations (COHP)[67] are computed for the title structures to estimate the bonding type between the constituent atoms and their strength. Fig. 10 shows the −COHP (E) and integrated-COHP plots for $Sr_3Zr_2Cu_4S_9$. The −ICOHP values suggest that the bond strength between atom pairs varies in the order Zr–S > Cu–S > Cu–Zr > Sr–S. The COHP and ICOHP plots for $Sr_3Zr_2Cu_4Se_9$ are presented in Fig. S5 in ESI† and indicate a similar order for bonding strengths.

We next discuss the computed Bader charges (Q_B) of the atoms in the $Sr_3Zr_2Cu_4Q_9$ structures. In general, the magnitudes of the Bader charges are smaller than the formal oxidation states of atoms since the latter values are calculated by considering the full charge transfer from metals (cations) to non-metals (anions), *i.e.*, considering the crystalline inorganic solids as perfect ionic compounds. The Q_B values provide estimates of the relative charge transfer between atom pairs and the degree of ionic/covalent character of the bonds.[68] For $Sr_3Zr_2Cu_4S_9$, these charges are +1.54, +2.02, +0.39, and −1.16 for Sr, Zr, Cu, and S ions, respectively. Likewise, in $Sr_3Zr_2Cu_4Se_9$, Q_B values of +1.49, +1.87, +0.35, and −1.10 were found for the Sr, Zr, Cu, and Se ions, respectively. Indeed, the magnitudes of the computed Q_B values are smaller than the formal oxidation states +II, +IV, +I, and −II for the Sr, Zr, Cu, and S (Se) ions. The deviation of Q_B values of the atoms, especially Zr, Cu, and S, in the $Sr_3Zr_2Cu_4Q_9$ structures from their formal oxidation numbers indicate the partial covalent character of the metal–chalcogen bonds due to the overlapping of orbitals, as discussed earlier.

4. Conclusions

The single crystals and polycrystals of two new quaternary mixed metal chalcogenides, $Sr_3Zr_2Cu_4S_9$ and $Sr_3Zr_2Cu_4Se_9$, were successfully prepared by reacting elemental reactants at high temperatures under vacuum. The SCXRD studies of the prepared quaternary crystals are carried out at RT, revealing that $Sr_3Zr_2Cu_4Se_9$ adopts a new structure type. The selenide phase is non-stoichiometric due to Cu-deficiency in the structure. On the contrary, the isoelectronic sulfide, $Sr_3Zr_2Cu_4S_9$, is stoichiometric and crystallizes in the $Ba_3Zr_2Cu_4S_9$ structure type. The triclinic structures (space group: $P\bar{1}$) of both $Sr_3Zr_2Cu_4Q_9$ phases are pseudo-two-dimensional, containing layers of $^{\infty}_{2}[Zr_2Cu_4Q_9]^{6-}$. The two structures differ in the coordination geometries of their Cu atoms. For the sulfur analog, there are tetrahedral CuS_4 units and trigonal CuS_3 units, and for the selenide structure, only tetrahedrally coordinated Cu atoms are present in the structure. The optical absorption study of the red-colored $Sr_3Zr_2Cu_4S_9$ sample yields a direct bandgap of 1.7(1) eV. The resistivity study of the selenide, $Sr_3Zr_2Cu_4Se_9$, shows a temperature dependence typical for a semimetal/degenerate semiconductor. Also, the *p*-type nature of the $Sr_3Zr_2Cu_4Se_9$ sample is established from the Seebeck study. The photovoltaic behavior of the $Sr_3Zr_2Cu_4S_9$ powder was studied by using it as a co-sensitizer in a CdS-based solar cell, which increased the overall efficiency by ~24%. The DFT studies were used to calculate the electronic structures of $Sr_3Zr_2Cu_4Q_9$. The theoretical analysis of the band structure of the $Sr_3Zr_2Cu_4S_9$ phase shows the direct bandgap nature of the sulfide and it is consistent with the experimental studies. The COHP, ICOHP, and Bader charge calculation studies suggest the bonding interactions between Zr/Cu and S atoms are stronger than the Sr–S interactions.

Data availability

Electronic supplementary information (ESI) is available, providing additional crystallographic details of the $Sr_3Zr_2Cu_4S_9$ and $Sr_3Zr_2Cu_4Se_9$ structures. The CIF files for these structures have been deposited with the joint CCDC/FIZ Karlsruhe deposition service under CSD numbers 2390675 and 2390676, respectively.†

Conflicts of interest

The authors declare that they have no known competing financial interests or personal relationships that could have appeared to influence the work reported in this article.

Acknowledgements

JP thanks DST-SERB, the Government of India (GOI) for the financial support under the core research grant (Grant Number: CRG/2021/0003641), and IIT Hyderabad for research facilities. SB and SY thank MOE and GOI for the Prime Minister Research Fellowship (PMRF). AKR thanks DST, India, for the INSPIRE fellowship, and Swati thanks CSIR for the Senior Research Fellowship. The authors are thankful to DST-FIST(SR/FST/PSI-215/2016) for computational resources. The authors also acknowledge Dr Surya Jammalamadaka from the Department of Physics at IIT Hyderabad for his help with electrical resistivity data collection.

References

1 C. D. Malliakas, D. Y. Chung, H. Claus and M. G. Kanatzidis, *J. Am. Chem. Soc.*, 2016, **138**, 14694–14698.
2 Y. Kamihara, T. Watanabe, M. Hirano and H. Hosono, *J. Am. Chem. Soc.*, 2008, **130**, 3296–3297.
3 A. Le Donne, V. Trifiletti and S. Binetti, *Front. Chem.*, 2019, **7**, 297.

4 D. Shin, T. Zhu, X. Huang, O. Gunawan, V. Blum and D. B. Mitzi, *Adv. Mater.*, 2017, **29**, 1606945.
5 M. Chauhan, K. Soni, P. E. Karthik, K. P. Reddy, C. S. Gopinath and S. Deka, *J. Mater. Chem. A*, 2019, **7**, 6985–6994.
6 J. Deng, W. Yuan, P. Ren, Y. Wang, D. Deng, Z. Zhang and X. Bao, *RSC Adv.*, 2014, **4**, 34733–34738.
7 Y. Shi, A. Assoud, S. Ponou, S. Lidin and H. Kleinke, *J. Am. Chem. Soc.*, 2018, **140**, 8578–8585.
8 A. Assoud, N. Soheilnia and H. Kleinke, *Intermetallics*, 2007, **15**, 371–376.
9 V. V. Atuchin, F. Liang, S. Grazhdannikov, L. I. Isaenko, P. G. Krinitsin, M. S. Molokeev, I. P. Prosvirin, X. Jiang and Z. Lin, *RSC Adv.*, 2018, **8**, 9946–9955.
10 Z.-H. Kang, J. Guo, Z.-S. Feng, J.-Y. Gao, J.-J. Xie, L.-M. Zhang, V. Atuchin, Y. Andreev, G. Lanskii and A. Shaiduko, *Appl. Phys. B*, 2012, **108**, 545–552.
11 A. H. Reshak, V. V. Atuchin, S. Auluck and I. V. Kityk, *J. Phys.: Condens. Matter*, 2008, **20**, 325234.
12 V. P. Sachanyuk, G. P. Gorgut, V. V. Atuchin, I. D. Olekseyuk and O. V. Parasyuk, *J. Alloys Compd.*, 2008, **452**, 348–358.
13 Y. Han, H. Yi, Y. Wang, Z. Li, X. Chu and J.-H. Jiang, *ACS Nano*, 2022, **16**, 19053–19066.
14 V. Singh, K. S. Rawat, S. Mishra, T. Baghel, S. Fatima, A. A. John, N. Kalleti, D. Singh, A. Nazir, S. K. Rath and A. Goel, *J. Mater. Chem. B*, 2018, **6**, 3366–3371.
15 A. Rydosz, *Coatings*, 2018, **8**, 425.
16 Z. Ibupoto, K. Khun, V. Beni, X. Liu and M. Willander, *Sensors*, 2013, **13**, 7926–7938.
17 B. S. Sengar, V. Garg, A. Kumar, V. Awasthi, S. Kumar, V. V. Atuchin and S. Mukherjee, *Opt. Mater.*, 2018, **84**, 748–756.
18 V. Garg, B. S. Sengar, G. Siddharth, S. Kumar, V. V. Atuchin and S. Mukherjee, *Surf. Interfaces*, 2021, **25**, 101146.
19 R. Mulla and M. H. K. Rabinal, *Energy Technol.*, 2019, **7**, 1800850.
20 O. V. Parasyuk, V. V. Atuchin, Y. E. Romanyuk, L. P. Marushko, L. V. Piskach, I. D. Olekseyuk, S. V. Volkov and V. I. Pekhnyo, *J. Cryst. Growth*, 2011, **318**, 332–336.
21 H. Liu, X. Shi, F. Xu, L. Zhang, W. Zhang, L. Chen, Q. Li, C. Uher, T. Day and G. J. Snyder, *Nat. Mater.*, 2012, **11**, 422–425.
22 K. S. Weldert, W. G. Zeier, T. W. Day, M. Panthöfer, G. J. Snyder and W. Tremel, *J. Am. Chem. Soc.*, 2014, **136**, 12035–12040.
23 J. L. Niedziela, D. Bansal, A. F. May, J. Ding, T. Lanigan-Atkins, G. Ehlers, D. L. Abernathy, A. Said and O. Delaire, *Nat. Phys.*, 2019, **15**, 73–78.
24 X. Wang, P. Qiu, T. Zhang, D. Ren, L. Wu, X. Shi, J. Yang and L. Chen, *J. Mater. Chem. A*, 2015, **3**, 13662–13670.
25 C. Sturm, N. Boccalon, A. Assoud, T. Zou, J. Kycia and H. Kleinke, *Inorg. Chem.*, 2021, **60**, 12781–12789.
26 T. P. Bailey, S. Hui, H. Xie, A. Olvera, P. F. P. Poudeu, X. Tang and C. Uher, *J. Mater. Chem. A*, 2016, **4**, 17225–17235.
27 O. Mayasree, C. R. Sankar, Y. Cui, A. Assoud and H. Kleinke, *Eur. J. Inorg. Chem.*, 2011, **2011**, 4037–4042.
28 N. O. Azarapin, A. S. Aleksandrovsky, V. V. Atuchin, T. A. Gavrilova, A. S. Krylov, M. S. Molokeev, S. Mukherjee, A. S. Oreshonkov and O. V. Andreev, *J. Alloys Compd.*, 2020, **832**, 153134.
29 N. O. Azarapin, V. V. Atuchin, N. G. Maximov, A. S. Aleksandrovsky, M. S. Molokeev, A. S. Oreshonkov, N. P. Shestakov, A. S. Krylov, T. M. Burkhanova, S. Mukherjee and O. V. Andreev, *Mater. Res. Bull.*, 2021, **140**, 111314.
30 A. Choudhury, S. Mohapatra, H. Yaghoobnejad Asl, S. H. Lee, Y. S. Hor, J. E. Medvedeva, D. L. McClane, G. E. Hilmas, M. A. McGuire, A. F. May, H. Wang, S. Dash, A. Welton, P. Boolchand, K. P. Devlin, J. Aitken, R. Herbst-Irmer and V. Petříček, *J. Solid State Chem.*, 2017, **253**, 192–201.
31 C. C. Laing, B. E. Weiss, K. Pal, M. A. Quintero, H. Xie, X. Zhou, J. Shen, D. Y. Chung, C. Wolverton and M. G. Kanatzidis, *Chem. Mater.*, 2022, **34**, 8389–8402.
32 X. Yu, Z. Wang, P. Cai, K. Guo, J. Lin, S. Li, J. Xing, J. Zhang, X. Yang and J.-T. Zhao, *Inorg. Chem.*, 2024, **63**, 20093–20101.
33 C. Coughlan, M. Ibáñez, O. Dobrozhan, A. Singh, A. Cabot and K. M. Ryan, *Chem. Rev.*, 2017, **117**, 5865–6109.
34 R. Xu, S. Lai, Y. Zhang and X. Zhang, *Nanomaterials*, 2024, **14**, 832.
35 D. Shin, B. Saparov, T. Zhu, W. P. Huhn, V. Blum and D. B. Mitzi, *Chem. Mater.*, 2016, **28**, 4771–4780.
36 W. Arndt, H. Dittrich and H. W. Schock, *Thin Solid Films*, 1985, **130**, 209–216.
37 B. Yang, L. Wang, J. Han, Y. Zhou, H. Song, S. Chen, J. Zhong, L. Lv, D. Niu and J. Tang, *Chem. Mater.*, 2014, **26**, 3135–3143.
38 O. Shahid, S. Yadav, D. Maity, M. Deepa, M. K. Niranjan and J. Prakash, *New J. Chem.*, 2023, **47**, 5378–5389.
39 S. Chander, S. K. Tripathi, I. Kaur and A. K. De, *Mater. Today Sustain.*, 2024, **25**, 100662.
40 P. Jackson, D. Hariskos, R. Wuerz, O. Kiowski, A. Bauer, T. M. Friedlmeier and M. Powalla, *Phys. Status Solidi RRL*, 2015, **9**, 28–31.
41 K. Srivastava, O. Shahid, A. K. Ray, M. Deepa, M. K. Niranjan and J. Prakash, *J. Phys. Chem. Solids*, 2024, **192**, 112085.
42 K. Srivastava, O. Shahid, A. K. Ray, M. Deepa, M. K. Niranjan and J. Prakash, *J. Solid State Chem.*, 2023, **328**, 124344.
43 S. Maier, J. Prakash, D. Berthebaud, O. Perez, S. Bobev and F. Gascoin, *J. Solid State Chem.*, 2016, **242**, 14–20.
44 A. A. Coelho, *J. Appl. Crystallogr.*, 2018, **51**, 210–218.
45 *APEX3: Program for Data Collection on Area Detectors*, Bruker AXS Inc., Madison, WI, USA, 2016.
46 G. M. Sheldrick, *Acta Crystallogr.*, 2008, **64**, 112–122.
47 G. M. Sheldrick, *SADABS, Department of Structural Chemistry*, University of Göttingen, Göttingen, Germany, 2008.
48 S. Barman, S. Jana, G. Panigrahi, S. Yadav, M. K. Niranjan and J. Prakash, *New J. Chem.*, 2022, **46**, 15976–15986.

49 L. M. Gelato and E. Parthé, *J. Appl. Crystallogr.*, 1987, **20**, 139–143.
50 A. L. Spek, *J. Appl. Crystallogr.*, 2003, **36**, 7–13.
51 G. Kortüm, in *Reflectance Spectroscopy*, Springer Berlin Heidelberg, Berlin, Heidelberg, 1969, pp. 170–216.
52 R. Piazza, S. Buzzaccaro, E. Secchi and A. Parola, *Soft Matter*, 2012, **8**, 7112.
53 E. I. Andritsos, E. Zarkadoula, A. E. Phillips, M. T. Dove, C. J. Walker, V. V. Brazhkin and K. Trachenko, *J. Phys.: Condens. Matter*, 2013, **25**, 235401.
54 W. Kohn and L. J. Sham, *Phys. Rev.*, 1965, **140**, A1133–A1138.
55 G. Kresse and J. Furthmüller, *Phys. Rev. B:Condens. Matter Mater. Phys.*, 1996, **54**, 11169–11186.
56 W. Primak, H. Kaufman and R. Ward, *J. Am. Chem. Soc.*, 1948, **70**, 2043–2046.
57 J. Huster and W. Bronger, *Z. Anorg. Allg. Chem.*, 1999, **625**, 2033–2040.
58 A. V. Ruseikina, A. N. Pinigina, M. V. Grigoriev and D. A. Safin, *Cryst. Growth Des.*, 2024, **24**, 2485–2492.
59 H. M. Otte, *J. Appl. Phys.*, 1961, **32**, 1536–1546.
60 S. O. Long, A. V. Powell, S. Hull, F. Orlandi, C. C. Tang, A. R. Supka, M. Fornari and P. Vaqueiro, *Adv. Funct. Mater.*, 2020, **30**, 1909409.
61 Z. Shu, C. Shen, A. Lu, X. Gu and Z. Liu, *Crystals*, 2021, **11**, 1495.
62 F. Alahmari, S. Dey, A.-H. Emwas, B. Davaasuren and A. Rothenberger, *J. Alloys Compd.*, 2019, **776**, 1041–1047.
63 A. Pfitzner, *Z. Anorg. Allg. Chem.*, 1995, **621**, 685–688.
64 M. F. Mansuetto, P. M. Keane and J. A. Ibers, *J. Solid State Chem.*, 1992, **101**, 257–264.
65 A. Yadav, P. Deshmukh, K. Roberts, N. Jisrawi and S. Valluri, *J. Phys. Commun.*, 2019, **3**, 105001.
66 R. M. Martin, *Electronic Structure: Basic Theory and Practical Methods*, Cambridge University Press, 2020.
67 V. L. Deringer, A. L. Tchougréeff and R. Dronskowski, *J. Phys. Chem. A*, 2011, **115**, 5461–5466.
68 W. Tang, E. Sanville and G. Henkelman, *J. Phys.: Condens. Matter*, 2009, **21**, 084204.